Combined Metal-like Ductility and High Hardness in N-rich HfN Thin Films by Point Defect Superstructuring

Marcus Lorentzon[a], Davide Sangiovanni[b], Naoki Takata[c], Tianqi Zhu[c], Justinas Palisaitis[a], Lars Hultman[a, d], Jens Birch[a], Naureen Ghafoor[a]

[a] Thin Film Physics Division, Department of Physics, Chemistry and Biology (IFM), Linköping University, Sweden

[c] Theoretical Physics Division, Department of Physics, Chemistry and Biology (IFM), Linköping University, Sweden

[c] Department of Materials Process Engineering, Graduate School of Engineering, Nagoya University, Japan

[d] Center for Plasma and Thin Film Technologies, Ming Chi University of Technology, New Taipei City 24301, Taiwan

1. Chemical Composition by ToF-ERDA and RBS

A reliable analysis of the chemical composition of HfN presents some challenges. In this work, we are using the highly sensitive and accurate ion beam analysis techniques, Time-of-Flight Elastic Recoil Detection Analysis (ToF-ERDA) and Rutherford Backscattering Spectrometry (RBS). However, the large mass difference between the Hf and N atom poses a challenge as ToF-ERDA is more sensitive and accurate for light elements, while the opposite is the case for RBS.

Thus, we have used a combination of the two techniques. ToF-ERDA suffers from a high level of multiple scattering due to scattering on the heavy Hf atoms. This can be seen in the counts of the histogram banana in Figure 1, e.g. above the surface and below the film-substrate interface (see N-signal), which is unphysical. A gradient is obtained in the calculated depth profile. On the other hand, it is possible to see that no element lighter than Ar was detected in the film, except a small O-signal from an ultra-thin surface oxide. The detection limit of ToF-ERDA for light elements is in the region of 0.5 at. %, indicating that no, or negligibly small, amounts of light elements, including C and O, were included in the film.

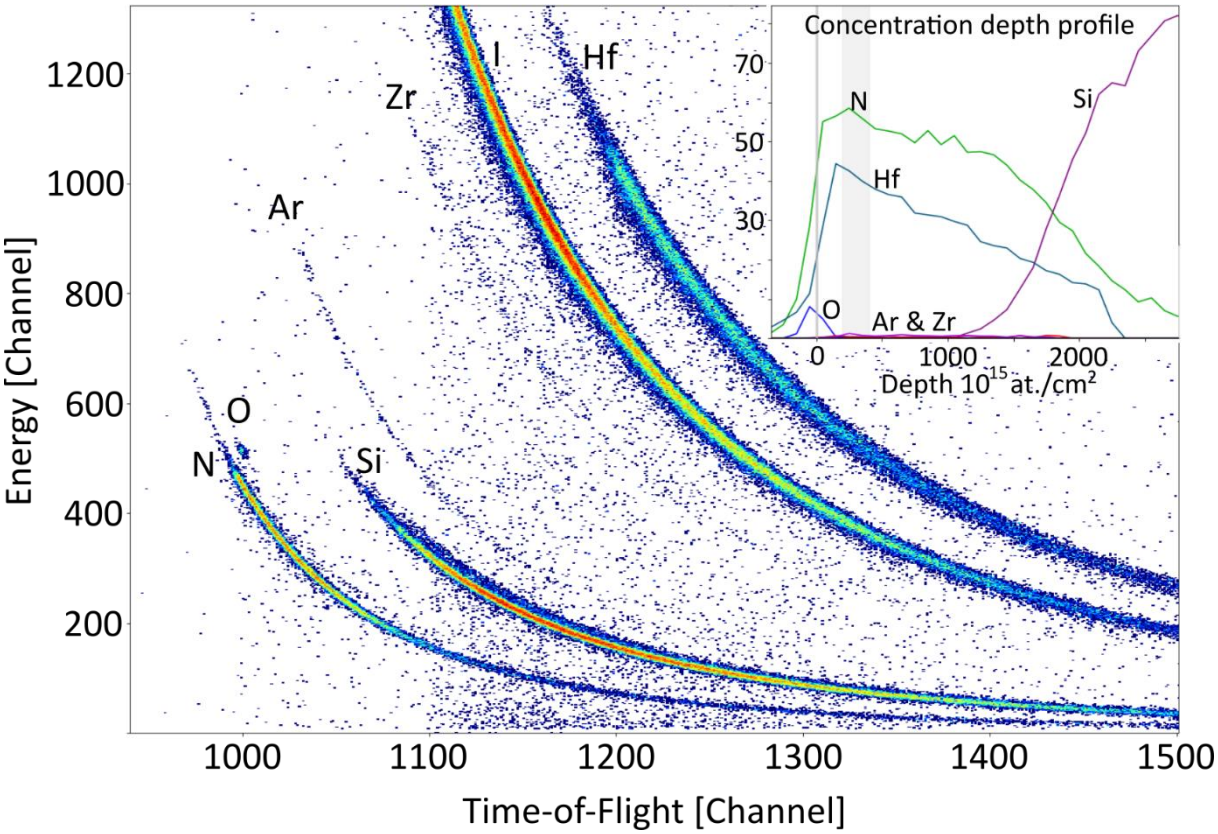

Figure 1: ToF-ERDA histogram and calculated depth profile inset for $HfN_{1.22}$ using the Potku code.

The information from ToF-ERDA was used in the RBS analysis which was the main tool to quantify the chemical composition. Quantification was done in SimNRA by fitting a simulation of the RBS spectra to the data. As seen in Figure 2, RBS is highly sensitive to heavy elements (intense Hf-signal), but light elements are often completely obscured by the substrate signal (N-signal). However, by knowing from ERDA that, for light elements, only N is present in the film, it becomes possible to quantify.

Background noise (stemming e.g. from multiple scattering) was simulated using a very heavy element (U in this case) in the substrate. The Ar, Zr, Hf, and substrate signals were then fitted to the data as shown in Figure 2, using a simulated homogeneous film target. The number of atoms in the Si substrate is set to 100%, (except ~0.04% U for simulating noise) which allows to determine the number of

incident ions on the sample. The fitting then provides the concentration of Hf, Zr and Ar, in number of atoms per area, or the percentage of these atoms in the film, and the missing atoms in order to sum up to 100% must therefore be N.

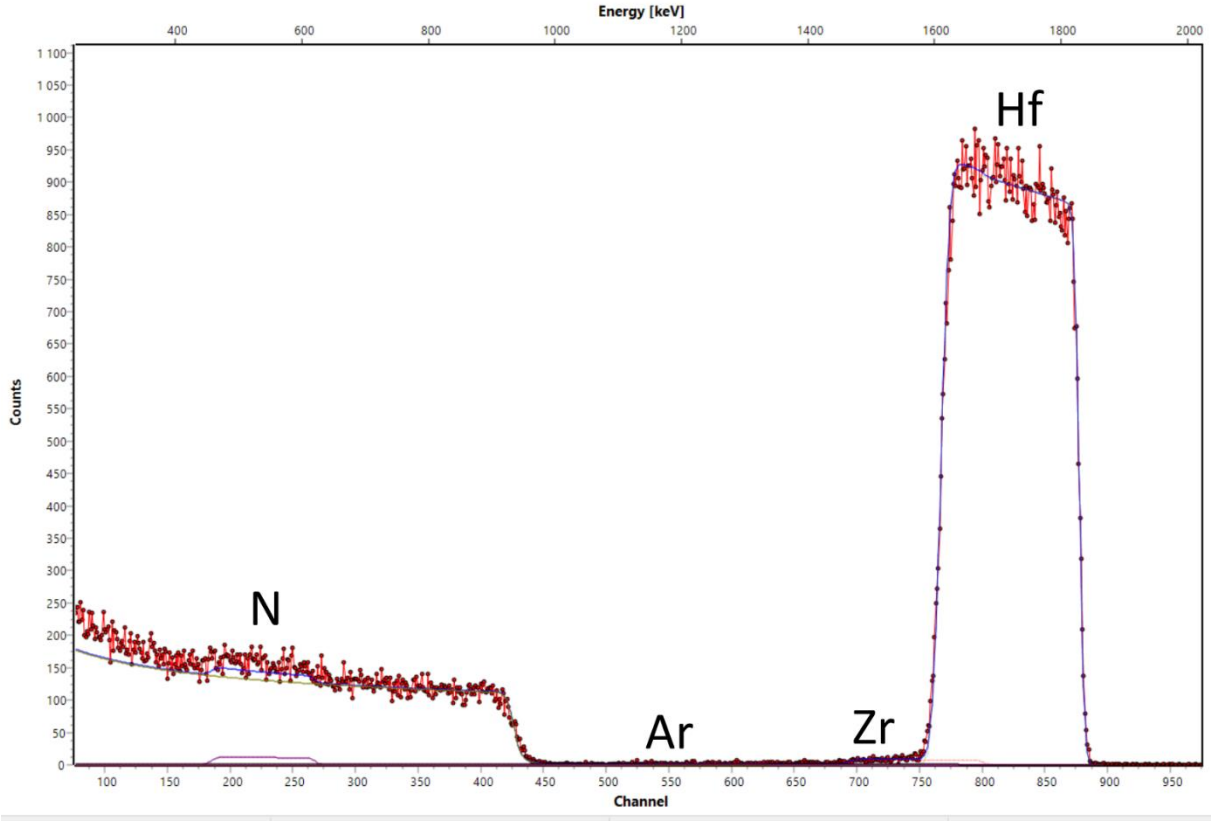

Figure 2: Experimental RBS spectrum (red) and simulation (blue) using the SimNRA code for $HfN_{1.22}$.

2. Structure of Films on Different Substrates

Figure 3 show XRD diffractograms of polycrystalline HfN_x, grown on Si(001) substrates with a native surface oxide, besides the epitaxial films which were presented in the main text. A very similar structure developed in the polycrystalline films with a high degree of (001) fiber texture along the surface normal, however small intensity peaks from (111), (220) (222), (331) and (420) were also detected, which likely originate from the early growth stages. The additional satellite peaks from the checkerboard superstructure, marked "S", are visible at the same 2θ angle as for the epitaxial films grown on MgO. Thus, the described superstructuring is independent of the film microstructure.

Ion assistance has been shown to substantially affect the morphology, texture and density of transition metal nitride films [1], [2], [3]. Ion assistance with a large ion-to-metal ratio (more than about 5) and low energy (less than about 20 eV) typically promotes a (001) fiber texture, compared to a dominant (111) texture for a less-energetic deposition conditions and without ion bombardment. Furthermore, the film density increases under ion bombardment, enhancing the mechanical properties.

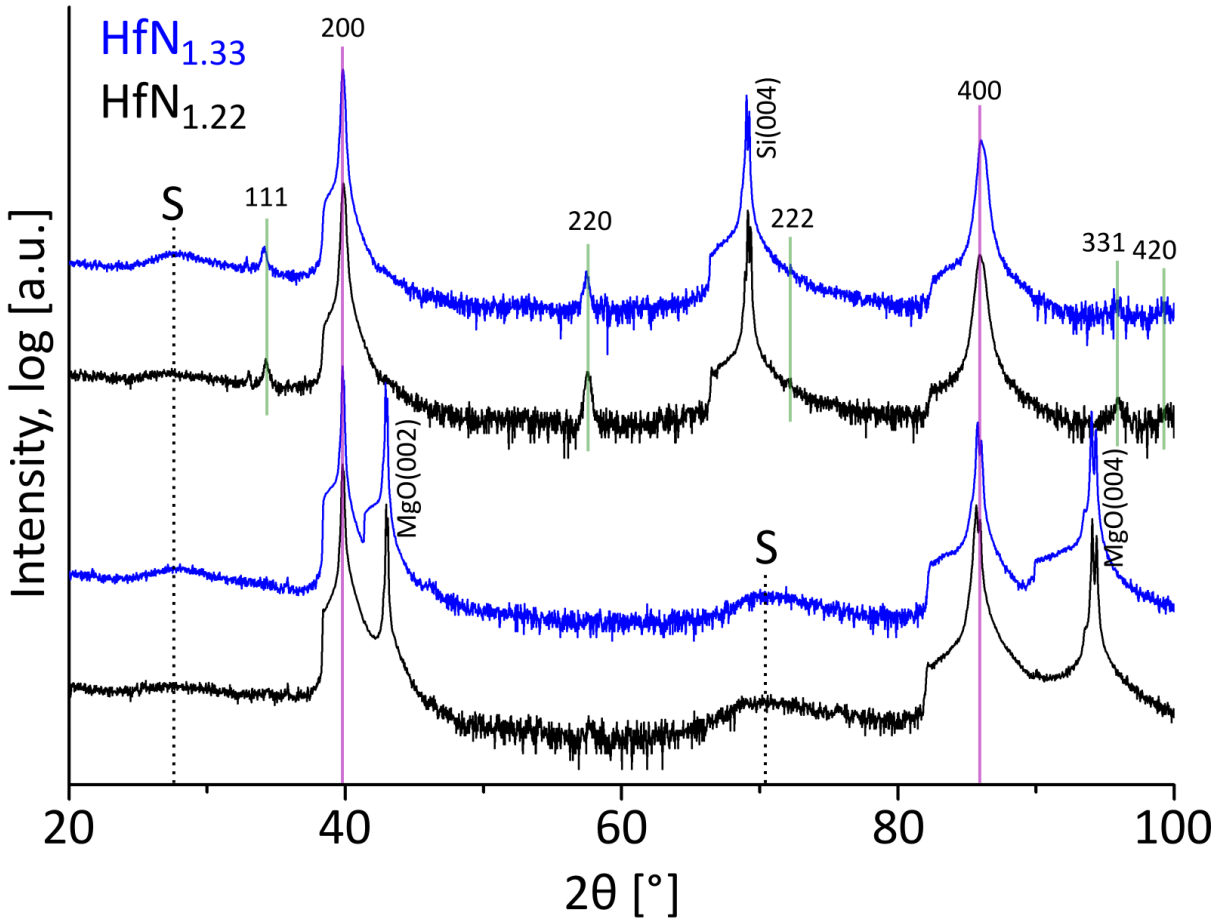

Figure 3: XRD θ–2θ scans from $HfN_{1.33}$ (blue) and $HfN_{1.22}$ (black) grown simultaneously on Si(001) substrates (top diffractograms) and MgO(001) substrates (bottom diffractograms). Diffraction peaks are marked by solid lines, and the superstructure peaks are marked by "S" and dotted lines.

3. Reciprocal Space Map Analysis

The film quality, relaxed lattice parameter and x-ray coherence lengths, $\xi_\perp$ and $\xi_\parallel$, were evaluated using high resolution reciprocal space maps (RSM). The maps were converted into Q-space using the measurement angles according to equations S1 and S2 [4].

$$Q_\perp = \frac{4\pi}{\lambda}\sin\theta\cos(\theta-\omega) = \frac{2\pi}{d_\perp}, \tag{S1}$$

$$Q_\parallel = \frac{4\pi}{\lambda}\sin\theta\sin(\theta-\omega) = \frac{2\pi}{d_\parallel}, \tag{S2}$$

The lateral and transverse lattice parameter was calculated as $a_\parallel = d_\parallel\sqrt{h^2+k^2}$ and $a_\perp = d_\perp\sqrt{l^2}$ which, for example, the $3\bar{1}\bar{1}$ peak results in: $a_\parallel = \sqrt{2}\,d_\parallel$ and $a_\perp = 3d_\perp$. The relaxed lattice parameter, a_0, was calculated according to equation S3 [5]. An assumed Poisson ratio, ν, of 0.25 was used [6].

$$a_0 = a_\perp\left(1 - \frac{2\nu(a_\perp - a_\parallel)}{a_\parallel(1+\nu)}\right), \tag{S3}$$

Besides the grazing exit $3\bar{1}\bar{1}$ reflection, 200 and $4\bar{2}0$ RSMs were measured, see Figure 4, as well as grazing incidence 311 and 420 RSMs (not shown). All HfN reciprocal lattice points exhibit a similar shape, i.e. substantially elongated along $Q_\parallel$ due to a small lateral x-ray coherence length (limited lateral size). However, also with a small tilt with respect to the horizontal direction corresponding to mosaicity. On the other hand, the points are relatively small in the transverse direction, representing a large transverse x-ray coherence length.

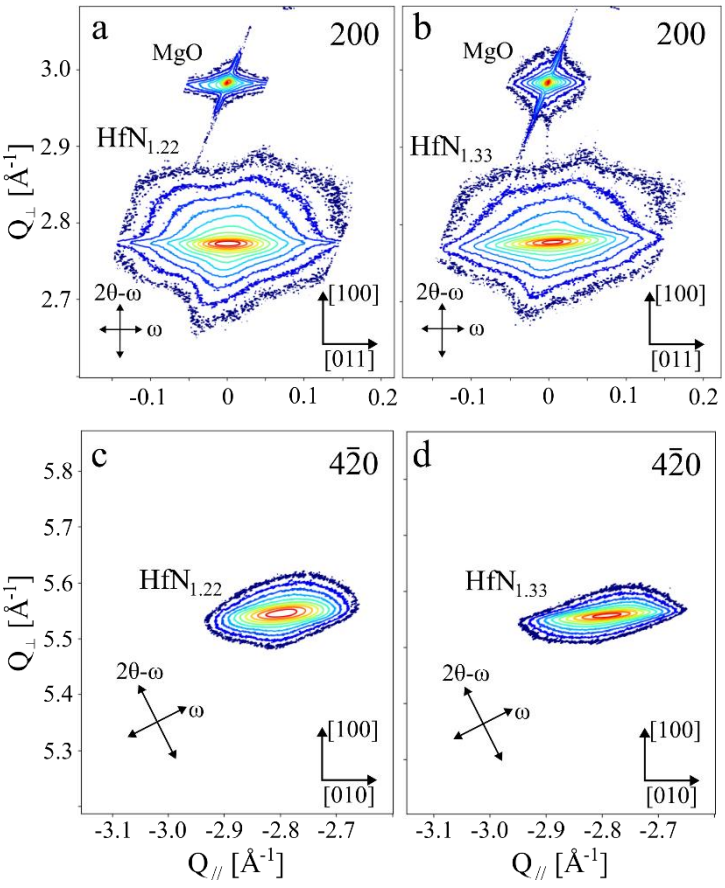

Figure 4: RSMs from both films with intensity plotted in logarithmic scale. a) and b) show the 200 RSMs and c) and d) show the $4\bar{2}0$ RSMs.

Linear plots with iso-intensity contour levels spaced according to $I_n^{contour} = \frac{I_{max}}{2^n}$ were used, where n-1 is the number of contours, and the max intensity point is at n = 0. As a result, the next outer contour represents half of the intensity of the closest inner contour. Therefore, the second (blue) contour corresponds to half of the maximum intensity, i.e. the full width at half maximum, FWHM. An example is shown in Figure 5a where both MgO and $HfN_{1.33}$ $3\bar{1}\bar{1}$ reciprocal lattice points are plotted in the same graph with a total of 8 contours. The outermost contour has an intensity of $I_7^{contour} = \frac{I_{max}}{64}$. The tilt of the reciprocal point with respect to the lateral direction was calculated according to Figure 5b, resulting in $\varphi = 5.23°$. A maximum value of 8.7° was measured from all RSMs, indicating that the peak broadening is dominated by the limited lateral size.

The limited lateral size, L, and mosaic tilt, α, was separated using the graphical method described by Moram and Vickers [7]. Figure 5c illustrates the process using the FWHM contour. The left and right points were placed on the edges of the elliptical contour. The middle point was found at the intersection between a horizontal line through the left point, and an ω-parallel line through the right point. Given the length of the lines, L and α were calculated according to Eq. S4 and S5.

$$L = \frac{2\pi}{\Delta Q_L} \tag{S4}$$

$$\alpha = \frac{\Delta Q_\omega}{Q} \tag{S5}$$

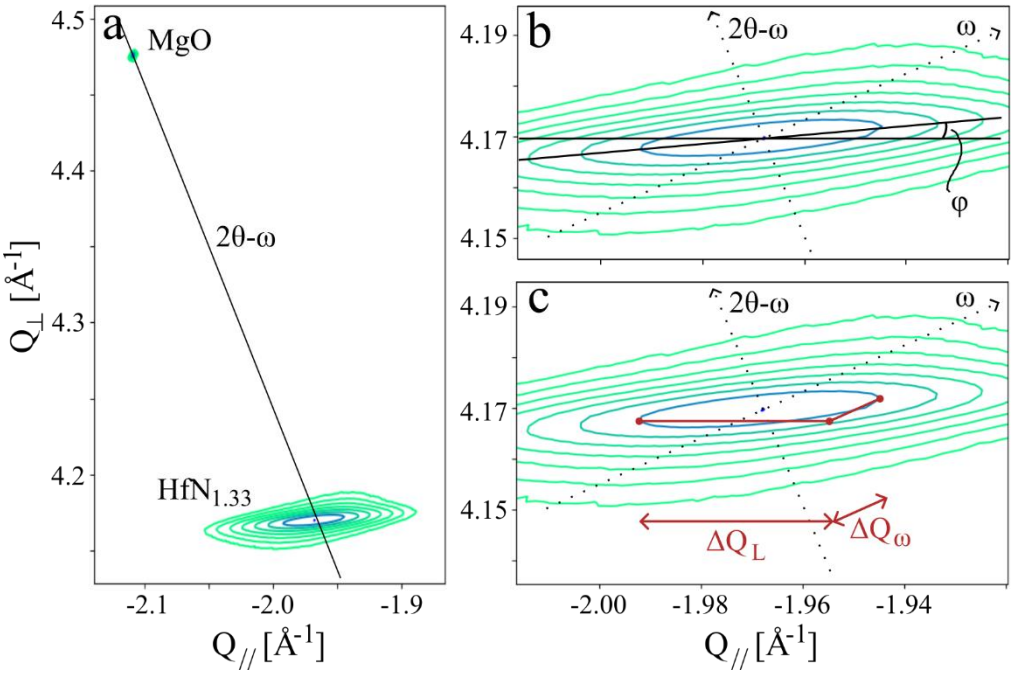

Figure 5: a) RSM of MgO and $HfN_{1.33}$ $3\bar{1}\bar{1}$ reciprocal lattice point. b) and c) zoomed-in image around the $HfN_{1.33}$ point. Dotted lines in b) mark the 2θ-ω and ω directions respectively while solid lines mark the angle between the horizontal line and tilted peak. Red solid lines in c) show the method of separation between limited lateral size and tilt.

The instrument broadening was accounted for using Equation S6, where the integral breath, β, were approximated using the FWHM. The instrument broadening was taken as the FWHM of the corresponding MgO peaks. The instrumental broadening was considerably smaller than the sample broadening, at least in the lateral direction: the maximal difference in L was <1.16% for $HfN_{1.22}$ and <0.54% for $HfN_{1.33}$.

$$\beta_G^2 = \beta_{sample}^2 + \beta_{instrument}^2 \quad \text{(S6)}$$

The results of the symmetric 200 and asymmetric grazing exit $3\bar{1}\bar{1}$ and $4\bar{2}0$ RSMs are presented in Table 1 and Table 2.

The grazing incidence RSMs were excluded from the analysis. For higher resolution and smaller wafer curvature effects, it is preferred to have a small beam footprint on the sample. In this case, a high enough intensity was obtained in grazing exit RSMs thanks to the relatively thick films, good quality crystals, and the strongly scattering Hf atoms. Furthermore, we observed that the scanning line mode of the detector was detrimental to the resolution when the beam footprint was too large.

Table 1: Calculated lattice parameters, lateral, $a_{\parallel}$, transverse, $a_{\perp}$, and relaxed, a_0, from different RSMs for $HfN_{1.22}$ and $HfN_{1.33}$.

Peak	$a_{\parallel}$ [Å]		$a_{\perp}$ [Å]		a_0 [Å]	
	$HfN_{1.22}$	$HfN_{1.33}$	$HfN_{1.22}$	$HfN_{1.33}$	$HfN_{1.22}$	$HfN_{1.33}$
200	0	0	4.532	4.526	-	-
$3\bar{1}\bar{1}$	4.560	4.515	4.517	4.521	4.534	4.519
$4\bar{2}0$	4.492	4.509	4.533	4.523	4.516	4.518
Average $3\bar{1}\bar{1}$ & $4\bar{2}0$	**-**	**-**	**-**	**-**	**4.525**	**4.518**

Table 2: Tilt angle, φ, limited lateral size, L, and tilt/twist, α, calculated from different RSMs for $HfN_{1.22}$ and $HfN_{1.33}$.

Peak	Tilt angle, φ [°]		Limited lateral size, L [Å]		Tilt/twist, α [°]		Tilt/twist, α [arcseconds]	
	$HfN_{1.22}$	$HfN_{1.33}$	$HfN_{1.22}$	$HfN_{1.33}$	$HfN_{1.22}$	$HfN_{1.33}$	$HfN_{1.22}$	$HfN_{1.33}$
200	-	-	196	182	-	-	-	-
$3\bar{1}\bar{1}$	8.7	5.2	216	164	0.192	0.126	690	455
$4\bar{2}0$	7.7	5.1	139	122	0.171	0.115	614	413
Average $3\bar{1}\bar{1}$ & $4\bar{2}0$	**8.2**	**5.2**	**177**	**143**	**0.181**	**0.121**	**652**	**434**

4. Complementary SAED and Bright-Field TEM

The cube-on-cube epitaxy of the $HfN_{1.33}$ film on MgO(001) substrate is evidenced in Figure 6. Due to the larger lattice parameter, the respective peak corresponding to the film is closer to 000, compared to the same peak for MgO.

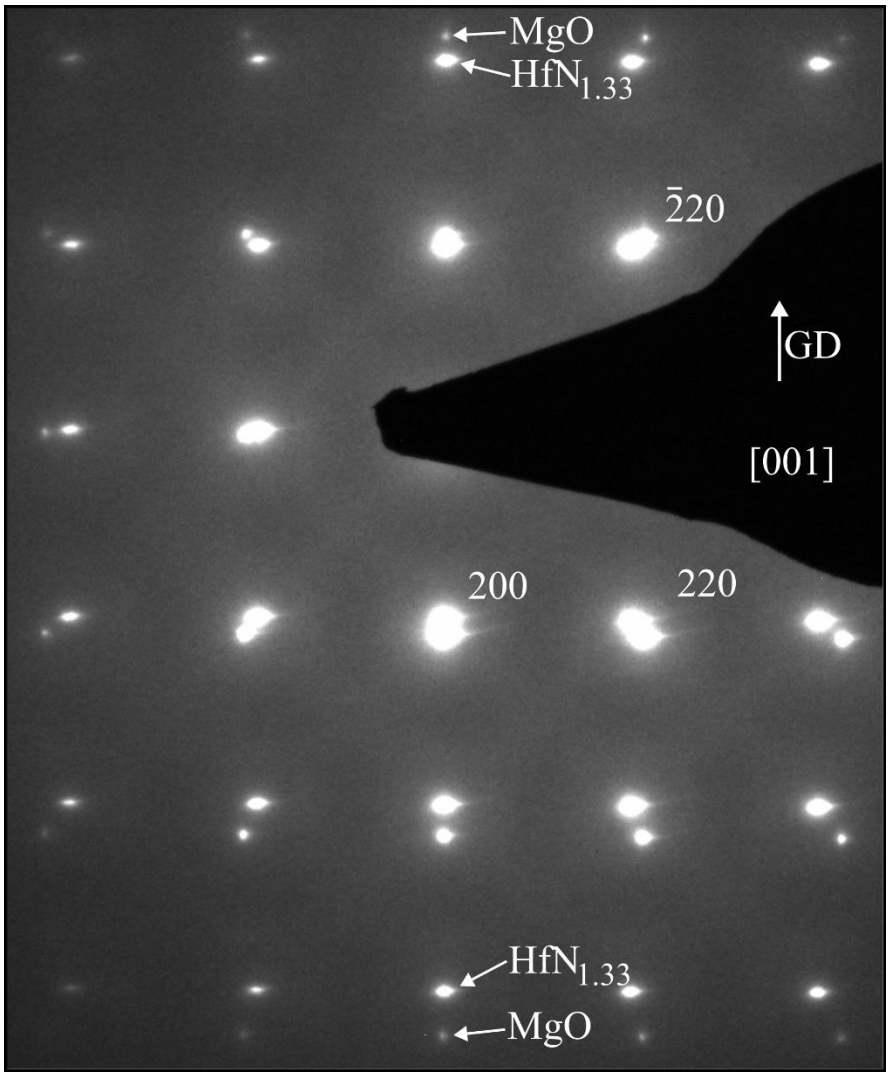

Figure 6: SAED pattern of both film and substrate peaks acquired simultaneously showing a cube-on-cube epitaxy.

Figure 7 show BF-TEM micrographs from three different areas, where Figure 7b is the same area as Fig.4 in the main text. Dislocations are often visualized using BF-TEM, why these images complement the ones in the main text. A large density of dislocations is clearly seen in all micrographs. The poor contrast in Figure 7a, c is due to a thicker area of the sample. We observe a larger thickness close to the substrate, due to ion milling effects of a hard coating on a soft substrate.

These BF-TEM images were acquired using a FEI Tecnai G2 microscope, operated at 200 kV, which given the highly scattering Hf-atom and the current thickness, is not enough to penetrate the sample as strongly as the 300 kV beam for STEM images in the main text.

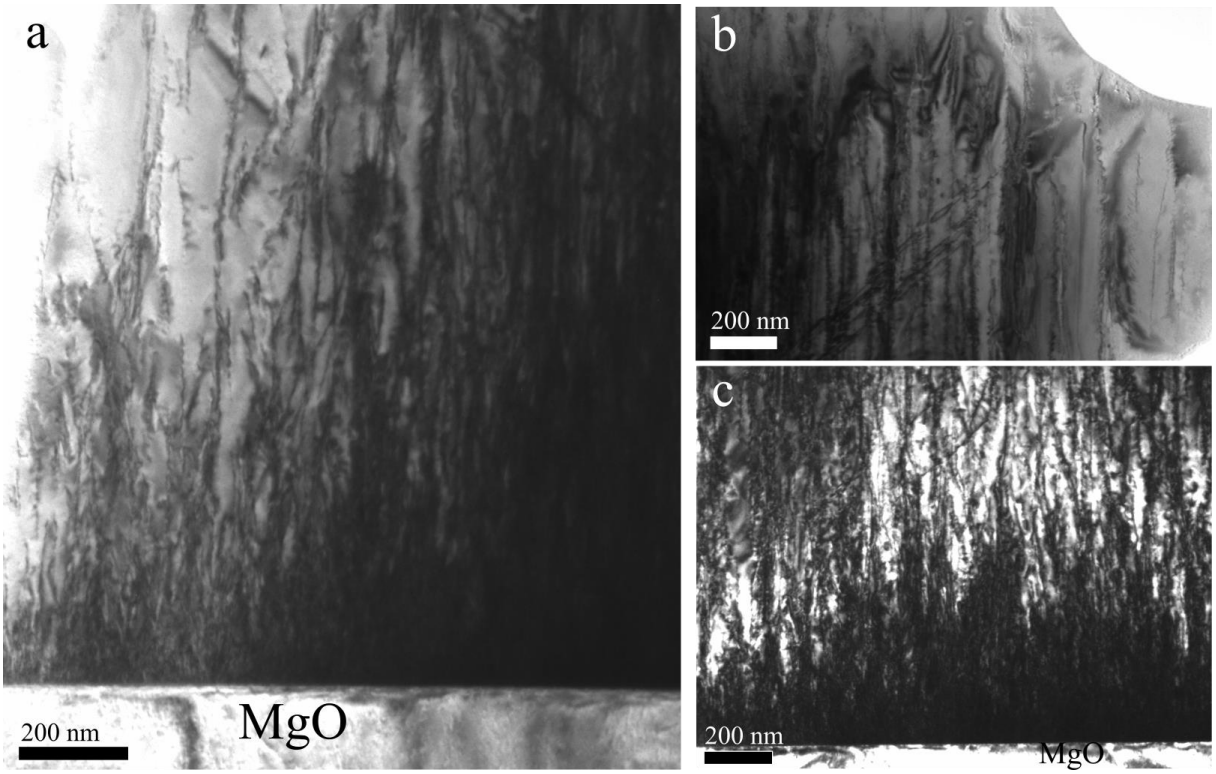

Figure 7: BF-TEM of $HfN_{1.22}$ where b) is imaged from the same area as in Figure 2 in the main text.

5. Ab-initio Calculations

To confirm reliability of MLIP results, the four structures shown in Figure 3a,b,c,d in the main text, are re-relaxed by DFT calculations. The DFT vs. MLIP differences in total energies are 7, 16, 1, and 17 meV/f.u., respectively. The corresponding average distances between relaxed atomic positions are 14, 22, 8, and 6 pm/atom, respectively. These relatively small deviations (in relation to the wide energy range shown in Figure 3e support validity of our analysis.

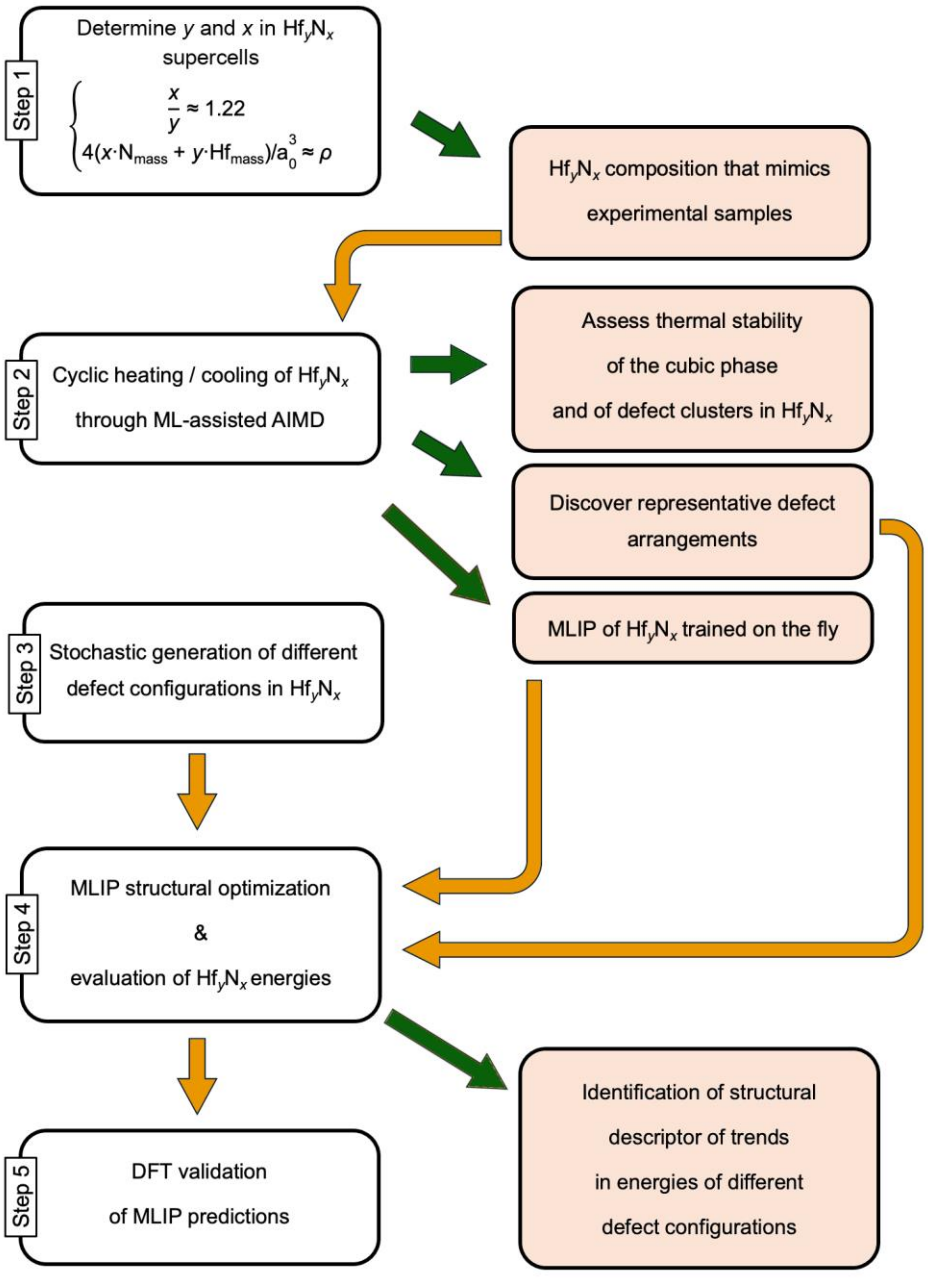

Figure 8: Workflow of ab initio and machine-learning modelling of Hf_xN_y. The tasks are divided in five Steps. Outputs of a task are indicated by green arrows in color-shaded boxes. Orange arrows indicate that the content of a box, or results of a task, serve as input for the next task. The final goal is to achieve an understanding of defect clustering based on energetics considerations.

Step 1 of Figure 8: The nanopatterning observed in $HfN_{1.22}$ films is studied via both DFT and AIMD. The Hf (y) and N (x) composition is mimicked with $Hf_{0.91}N_{1.10}$ (≡ $HfN_{1.22}$) supercells containing 98 Hf atoms (10 cation vacancies) and 119 N atoms (fully occupied anion sublattice + 11 N interstitials). Such composition is predicted based on the experimentally-determined stoichiometry (N/Hf = 1.22±0.03), relaxed lattice parameter (a_0 = 4.535 ± 0.020 Å), and density (ρ ≈12.6 $g \cdot cm^{-3}$) of $HfN_{1.22}$ samples.

Step 2 of Figure 8: AIMD simulations of $Hf_{0.91}N_{1.10}$ are accelerated by the aid of machine-learning (ML), which also enables on-the-fly training of a Hf-N interatomic potential (MLIP). We use 1-fs timesteps for integration of the nuclei equations of motion, with a total simulation time of ≈0.2 ns. We apply the velocity-rescaling algorithm to cyclically vary the simulation temperature between 300 and 2500 K and gain insights onto the thermal stability of defect clusters. Note that HfN melts at temperatures well above 3000 K. The heating/cooling rates are in a range between 30 and 60 K/ps.

Steps 3, 4, 5 of Figure 8: The MLIP prepared during ML-assisted AIMD simulations is then used to compute the energies of several different stochastic arrangements of 10 V_{metal} and 11 N-interstitials in $Hf_{0.91}N_{1.10}$ supercells. The approach is equivalent to Monte Carlo simple-sampling (MC) of the defect configurational space. The energies and relaxed atomic positions of four representative cases (two with lowest and two with highest energies) are also recomputed by DFT to validate the MLIP. As described in the results section, we identify a structural descriptor that well correlates with defect configuration energies. The descriptor allows us to interpret the tendency of overstoichiometric Hf_xN_y to form nanopatterned defect superstructures based on energetic arguments.

6. Micropillar Compression Testing

Compression testing of thin films requires small pillar dimensions due to the limited film thickness. Thus, a maximum pillar diameter of 1 to 2 μm is often used, giving a pillar ratio of at least 2:1. At such small dimensions, the well-known size effect [8], [9], [10] can become important, where the material strengthens with decreasing size thanks to a reduced number of defects in the sampling volume. In addition, the plasticity mechanisms might change, and the test is therefore not representative of the bulk material. In this work, however, reproducible and low scatter stress-strain curves were obtained, no sink-in and no critical fracture was observed. The intrinsic dislocation density is very high, resulting in a sound number of dislocations in respective $HfN_{1.22}$ pillar, which has been shown crucial for a representative results without significant size-effects [11]. For example, bulk-like behavior and small scatter in the stress-strain data was obtained in compression of metallic Mo pillars of a diameter of ~360nm, as long as sufficiently large dislocation density was first introduced in the as-grown pristine single crystal pillar by pre-straining [12]. Shen et at. recently reported substantial room temperature plasticity in brittle single crystals ceramics TiO_2 and Al_3O_2, by pre-straining the material at high temperatures, above the brittle-to-ductile transition [13]. Both these studies highlight the importance of the presence of large amounts of dislocations. Therefore, we believe that a true mechanical response of the $HfN_{1.22}$ film was measured and supports the interpretation of a unique ductile behavior of the hard material in this work.

The plastic deformation of the crystal structure of the compressed $HfN_{1.22}$ micropillar was measured by SAED as shown in Figure 9. In the diffraction pattern close to the substrate interface we observe discrete spots from the single crystal, indicating no plastic deformation in the lower half of the pillar. In contrast, in the top/middle of the pillar, the SAED pattern in Figure 9b has developed arcs, and the entire diffraction pattern is slightly tilted compared to Figure 9c which confirms the case of global plastic deformation. Additionally, very weak intensity surrounding each of the diffraction spots are seen in Figure 9c, which again supports the formation of a superstructure.

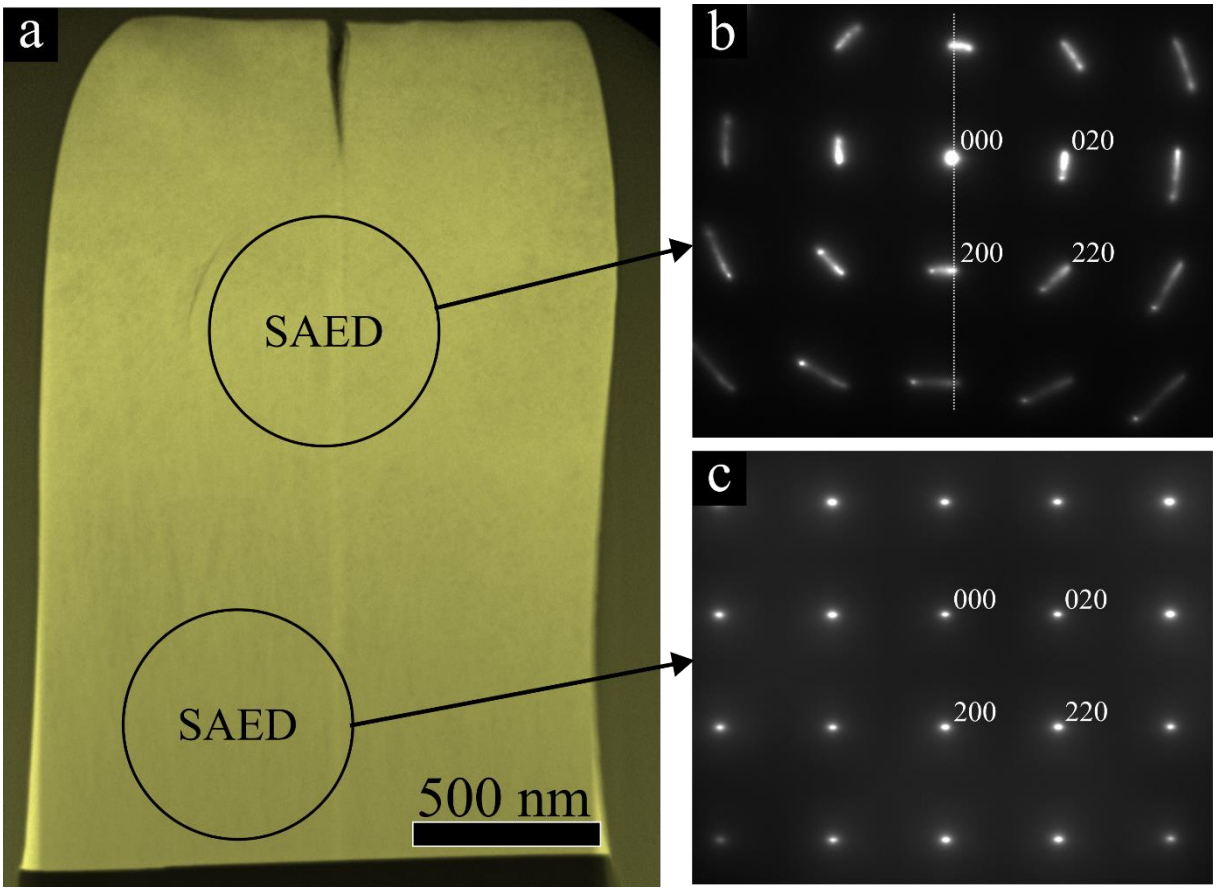

Figure 9: SAED patterns from two different positions marked in the pillar in a). From the top-center of the pillar in b) and from the bottom in c), where weak contrast from superstructured satellites are visible.

7. References

[1] I. Petrov, P. B. Barna, L. Hultman, and J. E. Greene, “Microstructural evolution during film growth,” *Journal of Vacuum Science & Technology A*, vol. 21, no. 5, pp. S117–S128, Sep. 2003, doi: 10.1116/1.1601610.

[2] D. Gall, I. Petrov, N. Hellgren, L. Hultman, J. E. Sundgren, and J. E. Greene, “Growth of poly- and single-crystal ScN on MgO(001): Role of low-energy N2+ irradiation in determining texture, microstructure evolution, and mechanical properties,” *Journal of Applied Physics*, vol. 84, no. 11, pp. 6034–6041, Dec. 1998, doi: 10.1063/1.368913.

[3] F. Adibi, I. Petrov, J. E. Greene, L. Hultman, and J. -E. Sundgren, “Effects of high-flux low-energy (20–100 eV) ion irradiation during deposition on the microstructure and preferred orientation of Ti0.5Al0.5N alloys grown by ultra-high-vacuum reactive magnetron sputtering,” *Journal of Applied Physics*, vol. 73, no. 12, pp. 8580–8589, Jun. 1993, doi: 10.1063/1.353388.

[4] P. van der Sluis, “Determination of strain in epitaxial semiconductor layers by high-resolution X-ray diffraction,” *J. Phys. D: Appl. Phys.*, vol. 26, no. 4A, p. A188, Apr. 1993, doi: 10.1088/0022-3727/26/4A/039.

[5] A. B. Mei *et al.*, “Physical properties of epitaxial ZrN/MgO(001) layers grown by reactive magnetron sputtering,” *Journal of Vacuum Science & Technology A: Vacuum, Surfaces, and Films*, vol. 31, no. 6, p. 061516, Nov. 2013, doi: 10.1116/1.4825349.

[6] H.-S. Seo, T.-Y. Lee, I. Petrov, J. E. Greene, and D. Gall, “Epitaxial and polycrystalline HfNx (0.8⩽x⩽1.5) layers on MgO(001): Film growth and physical properties,” *Journal of Applied Physics*, vol. 97, no. 8, p. 083521, Apr. 2005, doi: 10.1063/1.1870097.

[7] M. A. Moram and M. E. Vickers, “X-ray diffraction of III-nitrides,” *Rep. Prog. Phys.*, vol. 72, no. 3, p. 036502, Feb. 2009, doi: 10.1088/0034-4885/72/3/036502.

[8] M. D. Uchic, D. M. Dimiduk, J. N. Florando, and W. D. Nix, “Sample Dimensions Influence Strength and Crystal Plasticity,” *Science*, vol. 305, no. 5686, pp. 986–989, Aug. 2004, doi: 10.1126/science.1098993.

[9] O. Kraft, P. A. Gruber, R. Mönig, and D. Weygand, “Plasticity in Confined Dimensions,” *Annual Review of Materials Research*, vol. 40, no. 1, pp. 293–317, 2010, doi: 10.1146/annurev-matsci-082908-145409.

[10] R. Raghavan, C. Kirchlechner, B. N. Jaya, M. Feuerbacher, and G. Dehm, “Mechanical size effects in a single crystalline equiatomic FeCrCoMnNi high entropy alloy,” *Scripta Materialia*, vol. 129, pp. 52–55, Mar. 2017, doi: 10.1016/j.scriptamat.2016.10.026.

[11] G. Dehm, B. N. Jaya, R. Raghavan, and C. Kirchlechner, “Overview on micro- and nanomechanical testing: New insights in interface plasticity and fracture at small length scales,” *Acta Materialia*, vol. 142, pp. 248–282, Jan. 2018, doi: 10.1016/j.actamat.2017.06.019.

[12] H. Bei, S. Shim, G. M. Pharr, and E. P. George, “Effects of pre-strain on the compressive stress–strain response of Mo-alloy single-crystal micropillars,” *Acta Materialia*, vol. 56, no. 17, pp. 4762–4770, Oct. 2008, doi: 10.1016/j.actamat.2008.05.030.

[13] C. Shen *et al.*, “Achieving room temperature plasticity in brittle ceramics through elevated temperature preloading,” *Science Advances*, vol. 10, no. 16, p. eadj4079, Apr. 2024, doi: 10.1126/sciadv.adj4079.